CHEMISTRY OF MATERIALS

pubs.acs.org/cm

Article

Superconductivity–Electron Count Relationship in Heusler Phases—the Case of $LiPd_2Si$

Karolina Górnicka, Xin Gui, Juan R. Chamorro, Tyrel M. McQueen, Robert J. Cava, Tomasz Klimczuk,* and Michał J. Winiarski*

Cite This: *Chem. Mater.* 2024, 36, 1870–1879

Read Online

ACCESS | Metrics & More | Article Recommendations | Supporting Information

ABSTRACT: We report superconductivity in the full Heusler compound $LiPd_2Si$ (space group $Fm\bar{3}m$, No. 225) at a critical temperature of T_c = 1.3 K and a normalized heat capacity jump at T_c, $\Delta C/\gamma T_c$ = 1.1. The low-temperature isothermal magnetization curves imply type-I superconductivity, as previously observed in $LiPd_2Ge$. We show, based on density functional theory calculations and using the molecular orbital theory approach, that while $LiPd_2Si$ and $LiPd_2Ge$ share the Pd cubic cage motif that is found in most of the reported Heusler superconductors, they show distinctive features in the electronic structure. This is due to the fact that Li occupies the site which, in other compounds, is filled with an early transition metal or a rare-earth metal. Thus, while a simple valence electron count–property relationship is useful in predicting and tuning Heusler materials, inclusion of the symmetry of interacting frontier orbitals is also necessary for the best understanding.

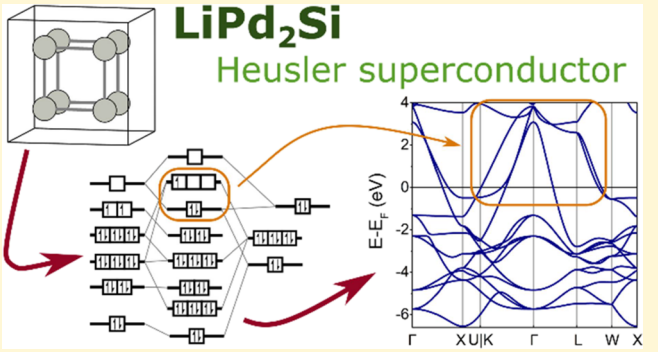

INTRODUCTION

At the beginning of the last century, Fritz Heusler studied various manganese alloys and found Mn_2CuAl—the first room-temperature ferromagnetic intermetallic compound that did not contain ferromagnetic elements.[1] While the discovery of a ferromagnet not containing any ferromagnetic element was considered remarkable by itself, it turned out to be just the tip of an iceberg. The Mn_2CuAl ("Full" Heusler) type is one of the most ubiquitous intermetallic structures[2−4] and has been dubbed as the *metallic equivalent of the perovskite*.[5] In addition, a number of closely related crystal structure types exist: the half Heusler (MgAgAs-type), inverse Heusler ($CuHg_2Ti$-type),[4] double half Heusler,[6] and LiMgPdSb-type[7,8] with a variety of chemical compositions and physical behaviors. The (full) Heusler intermetallic family is the fourth most common structure among more than 1000 structure types and more than 13,000 ternary intermetallic compounds.[2,5,9] A wide range of properties is observed in that vast group of compounds including half metallic ferromagnetism,[3,10,11] heavy Fermion behavior,[12−16] shape memory effect and mechanocaloric coupling,[17,18] and superconductivity.[19−23]

Full Heusler compounds form in the face-centered cubic crystal structure (space group $Fm\bar{3}m$, no. 225) and can be viewed as a NaCl-type lattice (strukturbericht B1), with the extra atoms filling all of its tetrahedral voids. In Mn_2CuAl, the sublattice is formed by Cu and Al atoms, and the voids are filled with Mn. Alternatively, the Heusler structure can also be seen as an ordered ternary variant of the CsCl-type cell (strukturbericht B2; see e.g., refs 4 and 24 or as a CaF_2-type ([anti]fluorite, strukturbericht C1).

A general formula for the full Heusler compounds is XY_2Z, where X and Y are usually transition metals and Z is a main-group element. In some compounds, X can be a rare earth element, alkaline (Li), or alkaline earth (Mg) metal. Within the unit cell, the eight Y atoms form a cubic cage, with each X atom neighboring six others (Figure 1a). Together the Z and Y_2 sublattices form a CaF_2-type Y_2Z structure, with voids filled by X atoms (or conversely a XY_2 structure with Z atoms filling the voids, as the X and Z sites (4*c* and 4*d*) are inequivalent but have the same symmetry.

Much of the diverse physical properties of the Heusler family can be rationalized within the framework of rigid band approximation and valence electron count (VEC). Within this simple approach, the electronic structure is assumed to be qualitatively robust toward changes in the elemental composition, and the difference between the properties thus stems from the change in the occupancy of different electronic

Received: September 19, 2023
Revised: January 30, 2024
Accepted: January 31, 2024
Published: February 15, 2024

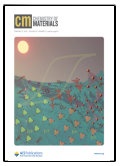

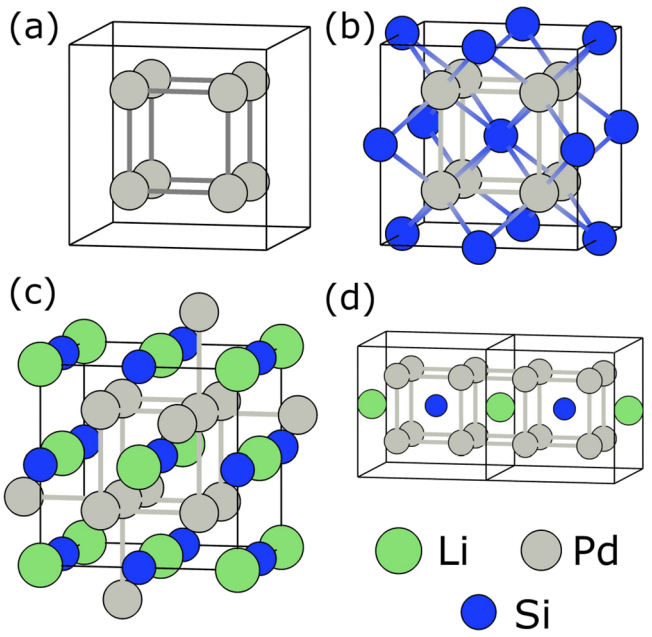

Figure 1. Crystal structure of a generic XY_2Z full Heusler phase can be described by considering first a $(Y_2)_4$ cubic cage (a) which interacts with a FCC sublattice Z (panel b), forming a CaF_2-type (strukturbericht C1) lattice. Full Heusler phase results from filling the voids of the CaF_2-type lattice with atom X (panel c). The resulting structure can also be viewed as two interpenetrating CaF_2-type networks (d). In $LiPd_2Si$, the voids of the CaF_2-type Pd_2Si sublattice are filled with Li atoms that play the role of electron donors. As we discuss further, the electronic structure of the full Heusler phase can be traced back to the molecular orbitals of the cubic cage formed by Y atoms.

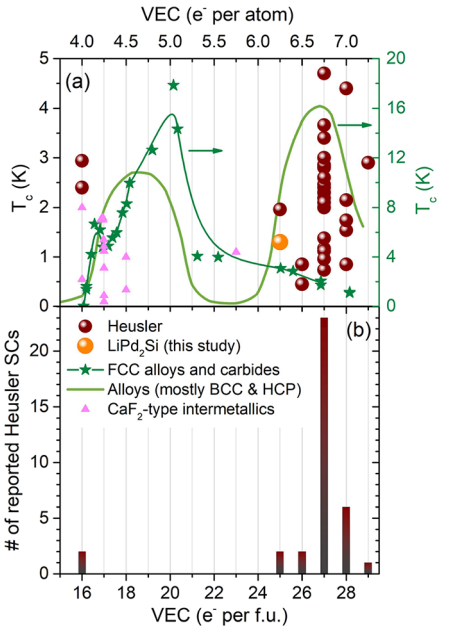

Figure 2. Panel (a) shows the highest reported T_c of Heusler superconductors for each VEC (brown spheres; $LiPd_2Si$ is shown in orange) compared to the reported T_c–VEC relationship in crystalline BCC alloys[33] (light green; data taken from ref 36), FCC alloys and carbides (dark green stars; line is added as a guide for eyes), and CaF_2-type intermetallics (pink triangles).[38] Panel (b) shows the number of reported Heusler superconductors vs valence electron count.[24,30,31]

states (i.e., the position of the Fermi level). While such a view is an obvious oversimplification, it is successful in explaining, for example, the effect of chemical doping on magnetic properties of Heusler compounds[4,5] and the stability of XYZ-XY_2Z half Heusler–full Heusler solid solutions.[25] The use of molecular orbital (MO) theory, or more precisely crystal orbital (CO) theory, allows one to put the relationship between VEC and the physical properties into the context of chemical bonding. An example of this approach is presented in the recent literature,[4] where it is explained that the exceptional stability and semiconducting properties of VEC = 8 and VEC = 18 half Heusler compounds by the closed shell configuration found for that electron count.[4] They also provide, on the same grounds, an explanation of the semiconducting properties of several VEC = 24 full Heusler compounds,[4] most notably VFe_2Al.[26−29]

We have previously shown that all but two of the 34 known Heusler superconductors have VEC = 25–29, and 70% (24 of 34) have VEC = 27. The highest reported T_c of a Heusler SC is also found at that electron count[19,24,30,31] (see Figure 2). In almost all of them, the X atom is a late *d*-block metal, i.e., Ni, Pd, Pt, and Au. Interestingly, VEC = 27 corresponds to 6.75 electrons per atom close to the second maximum of Matthias' empirical T_c–VEC relationship rule for pure elements and their alloys[32−34] (see Figure 2a) and to the maximum of T_c for α-Mn-type high-entropy alloys.[35,36] In our recent study, we reported superconductivity in $MgPd_2Sb$, the occurrence of which was predicted based on the compound's "magical" VEC = 27 electron count.[24] Recent machine learning predictions of superconductivity have also identified several Heusler compounds with similar electron counts as possible superconductors.[37]

Recently, we also studied a series of compounds $LiPd_2Z$ (Z = Si, Ge, Sn; VEC = 25) and found superconductivity in $LiPd_2Ge$ with T_c = 1.96 K.[39] The experimental results indicate that $LiPd_2Ge$ is a type-I weakly coupled BCS superconductor. Ab initio electron–phonon coupling calculations show a strong softening of the acoustic phonon mode in $LiPd_2Z$, and since the effect is most pronounced in $LiPd_2Ge$, we concluded that there is a correlation between superconductivity and a mode-softening effect. Our calculations predict superconductivity in two other members, $LiPd_2Si$ and $LiPd_2Sn$, with the expected T_c below 1 K in both cases.[39]

In this paper, we report low-temperature studies of the superconducting properties of $LiPd_2Si$—the second Heusler-type superconductor with VEC = 25. We also discuss its electronic structure and VEC in comparison to those of the remaining Heusler superconductors, highlighting the similarities and also pointing to the importance of changes in chemical bonding that violate the rigid band approximation.

EXPERIMENTAL DETAILS

Polycrystalline samples of $LiPd_2Si$ and $LiPd_2Sn$ were synthesized by the two-step solid-state reaction method that we reported previously.[39] Lithium chunks (Alfa Aesar, 99.99% pure), Pd powder (Mennica-Metale, Poland, 99.998%), Si pieces (Alfa Aesar, 99.9%), and Sn pellets (Alfa Aesar, 99.99%) were used as delivered without purification. Stoichiometric amounts of elemental reagents (with a 10% excess of Li to account for evaporative losses) were mixed and pressed into pellets using a hydraulic press inside a high-purity Ar-filled ($p(O_2)$ < 0.5 ppm) glovebox. The resulting pellets were placed in tantalum crucibles, covered with a piece of tantalum foil, and subsequently put in fused silica tubes that were evacuated, purged with argon gas, and backfilled with high-purity Ar prior to sealing (see

https://doi.org/10.1021/acs.chemmater.3c02398
Chem. Mater. 2024, 36, 1870−1879

Figure 3a). The use of a crucible cover and backfilling the ampules with Ar are necessary to avoid excessive Li evaporation during

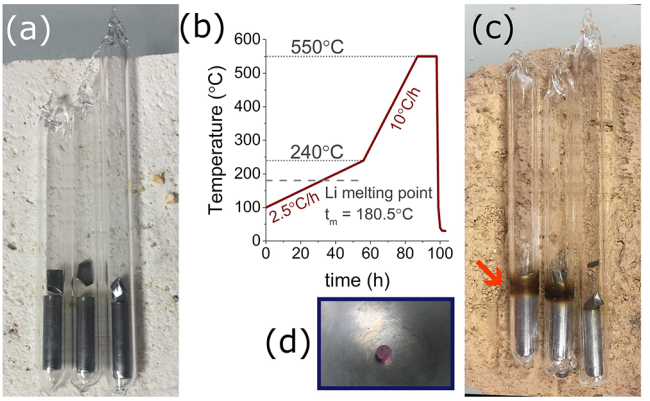

Figure 3. Panel (a) shows the ampules containing Ta crucibles loaded with pressed reagents (Li, Pd, and Si/Ge/Sn), capped with a piece of Ta foil. The heating procedure is shown in panel (b). Ampules after heating are shown in panel (c). Only a small discoloration due to the deposition of evaporated Li is seen on the tube walls. Panel (d) shows a resulting pellet of $LiPd_2Si$ with a brownish color. Results of measurements on the $LiPd_2Ge$ sample were recently presented in ref 39.

annealing (Figure 3c shows ampules after heating). The sealed tubes were then slowly heated at a rate of 2.5 °C/h from 100 to 240 °C (across the melting point of Li, t_m = 180.5 °C), then ramped at 10 °C/h to 550 °C, and soaked for 12 h (Figure 3b). Tubes were then air-quenched to room temperature and opened inside of the glovebox. Pellets were ground, repressed, and resealed in tubes, using the same Ta crucibles. The samples were then homogenized by annealing them at 610 °C over 3 days. The resulting dense, hard pellets were brownish in color (as previously reported for $LiPd_2Sn$;[40,41] see Figure 3d.

Heat capacity measurements employing the standard semiadiabatic pulse technique were conducted in the temperature range of 0.4−10 K using the ^{3}He−^{4}He option of the quantum design Dynacool physical property measurement system (PPMS). Magnetization measurements were performed with a QD MPMS-XL SQUID magnetometer in the temperature range of T = 0.4−1.8 K and in a magnetic field of up to $\mu_0 H$ = 0.5 T. Magnetization measurements performed on $LiPd_2Sn$ did not show any sign of superconducting transition down to T = 0.4 K, in agreement with our recent ab initio calculations.[39]

Resistivity measurement was performed on a polished fragment of a sample by means of the four-probe method, employing the ^{3}He option of the PPMS to achieve T < 2 K temperatures. Thin platinum wires were mounted on the sample surface using a conductive silver paste.

Density functional theory (DFT) calculations of the electronic structure of $LiPd_2Si$ were done using the Quantum Espresso 6.7MaX code,[42−44] employing the Perdew−Burke−Ernzerhof generalized gradient approximation (PBE GGA)[45] of the exchange−correlation potential in the scalar relativistic approximation (neglecting spin−orbit coupling). Projector augmented-wave[46,47] sets were taken from the PSlib[48] library. The charge density and kinetic energy cutoff values were set to 500 and 55 Ry, respectively. The unit cell dimension was relaxed using the BFGS method yielding a = 5.9542 Å, reasonably close to the experimental value (a = 5.9059 Å[39]). Crystal orbital Hamilton population[49,50] analysis was conducted using the Lobster 4.1.0 code[51,52] using the basis set by Koga et al.[53] for projections. Atomic charge analysis was performed using the BADER code.[54−56] For comparison, band structures of four Heusler phases (YPd_2In, $LuPt_2In$, $ZrNi_2Ga$, and $HfPd_2Al$) were taken from the Materials Project database[57] using the pymatgen module[58] and are shown in the Supporting Information (Figure S4).

RESULTS AND DISCUSSION

The existence of the title compound, the physical properties of which are described in this paper, was recently reported by us in ref 39. The powder XRD pattern of $LiPd_2Si$, together with the Rietveld structural analysis, is shown in Figure S1 of the Supporting Information. The profile refinement confirms a cubic $L2_1$ Heusler-type crystal structure (space group $Fm\bar{3}m$, No. 225) with the lattice parameter a = 5.9059(4) Å. Among the $LiPd_2Z$ series (Z = Si, Ge, Sn), $LiPd_2Si$ has the smallest unit cell, in agreement with the atomic radius trend of the tetrel elements.

To characterize the low-temperature behavior of $LiPd_2Si$, magnetic measurements were performed in different applied fields. Figure 4a displays the temperature dependence of the

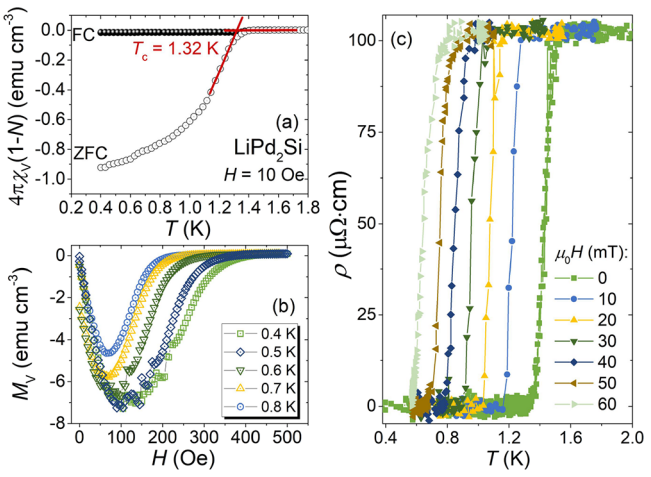

Figure 4. Panel (a) presents the temperature dependence of the volume magnetic susceptibility below 1.8 K, measured at 10 Oe with both ZFC and FC modes. Panel (b) shows field-dependent magnetization $M_V(H)$ measured below 500 Oe at various temperatures. Low-temperature resistivity measured at magnetic fields $\mu_0 H$ = 0 to 60 mT is shown in panel (c), showing an abrupt drop to zero at the critical temperature. See Figure S2 of the Supporting Information for resistivity data in a wider temperature range.

volume magnetic susceptibility χ_V(T), defined as $\chi_V = M/H$ (M—magnetization, H—applied magnetic field), upon both zero-field-cooled (ZFC) and field-cooled (FC) measurement modes in an applied low field of H = 10 Oe. The data are corrected for demagnetization effects and multiplied by 4π (here, a demagnetization factor of N = 0.58 is estimated from the $M_V(H)$ fit discussed later). An abrupt decrease of the magnetic susceptibility indicates the presence of a superconducting transition with T_c = 1.3 K, estimated as the point at which the extrapolation of the normal-state magnetic susceptibility intersects with the line set by the steepest slope of magnetization in the ZFC data set.[59] The critical temperature obtained for $LiPd_2Si$ is larger than that predicted by ab initio calculations (T_c = 0.76 K[39]). At the lowest available temperature, T = 0.4 K, the ZFC diamagnetic signal value of $4\pi\chi_V(1-N)$ is close to −1 and provides evidence for full Meissner screening in $LiPd_2Si$. A large difference between the FC and ZFC curves is frequently observed in polycrystalline superconducting samples.

The isothermal volume magnetization curves as a function of a magnetic field $M_V(H)$ measured for a range of temperatures ($0.4 \le T \le 0.8$ K) are displayed in Figure 4b. Assuming that

https://doi.org/10.1021/acs.chemmater.3c02398
Chem. Mater. 2024, 36, 1870−1879

the initial response to magnetic field is perfectly diamagnetic, the demagnetization factor $N = 0.58$ was found, consistent with the sample's shape used in the magnetic measurements. The $M_V(H)$ curves initially show a linear dependence on the magnetic field and then drop to zero near the critical field. This is not a rapid drop, which is expected for type-I superconductors. This may be caused by the occurrence of intermediate state due to sample shape effect (demagnetization factor) as well as sample inhomogeneity. A similar feature has been observed for isostructural and isoelectronic $LiPd_2Ge$ and other type-I superconductors, such as KBi_2,[60] $ScGa_3$,[61] $LuGa_3$,[61] LiBi,[62] and $ReAl_6$.[63]

Low-temperature resistivity $\rho(T)$ is shown in Figure 4c. A drop to zero is observed at the superconducting transition. The onset of the drop occurs at a temperature slightly higher than the one observed in the heat capacity and magnetization measurements. It is a typical behavior for a polycrystalline superconductor, as the drop of resistivity caused by the formation of a filamentary superconducting path usually occurs before the bulk of the sample becomes superconducting.

The residual resistivity ratio RRR = $\rho(300\ \text{K})/\rho_0$ (where ρ_0 is the residual resistivity just above the onset of superconducting transition; see Figure S2 of the Supporting Information) is 2.3, much lower than that measured for the $LiPd_2Ge$ sample (RRR = 14).[39] Although the RRR of different materials is not directly comparable, such a high difference may suggest the presence of a stronger structural disorder in the measured $LiPd_2Si$ sample.

To get important information about the superconducting transition, we carried out specific heat, $C_p(T)$, measurements at applied magnetic fields of both $\mu_0H = 0$ and 0.1 T. The inset of Figure 5a displays the temperature square dependence of C_p/T, under an applied magnetic field of $\mu_0H = 0.1$ T. In the normal state, in which bulk superconductivity is completely suppressed, the experimental data can be fitted using the formula $C_p/T = \gamma + \beta T^2$, where γ is the Sommerfeld coefficient ascribed to the electronic contribution and β is the phonon specific heat coefficient. The fit is shown as a solid red line and gives $\gamma = 5.3(1)$ mJ mol^{-1} K^{-2} and $\beta = 0.32(1)$ mJ mol^{-1} K^{-4}. The relatively low value of the Sommerfeld coefficient suggests weak electronic correlations. Then, the Debye temperature Θ_D was evaluated from β via a simple Debye model: $\Theta_D = \left(\frac{12\pi^4}{5\beta}nR\right)^{1/3}$, where $R = 8.31$ J mol^{-1}K^{-1} and $n = 2$,[39] yielding 230(3) K. The obtained values of γ and Θ_D are in good agreement with the previous report,[39] in which data were collected only down to $T = 1.8$ K. The main panel of Figure 5a shows the low-temperature specific heat $C_p/T(T)$ of $LiPd_2Si$ in zero magnetic field. The presence of a well-defined jump in specific heat indicates bulk superconductivity with $T_c = 1.3$ K, which is consistent with the value obtained from the magnetic measurements. The normalized specific heat jump at the critical temperature, $\Delta C/\gamma T_c$, is 1.1, slightly lower than the value expected by BCS theory (1.43).

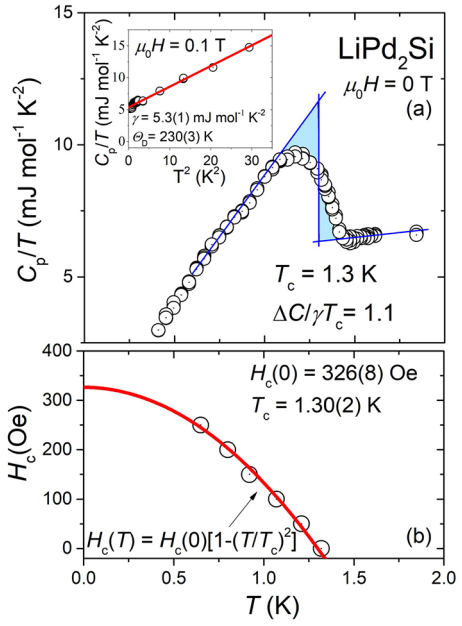

Figure 5. Panel (a) shows the temperature dependence of the specific heat in the vicinity of the superconducting transition. Equal entropy construction (blue lines) was used to estimate $T_c = 1.3$ K (in good agreement with magnetization results; see Figure 4). Inset: C_p/T vs T^2 measured in a 0.1 T applied magnetic field. The red solid line represents the linear fit used to estimate the values of the electronic and phonon specific heat coefficients. Panel (b) displays the critical field $H_c(T)$ determined from $C_p(T)$ (open circles).

Having the estimated Debye temperature Θ_D, the electron–phonon coupling constant $\lambda_{e\text{-}p}$ can be estimated from the inverted McMillan formula:[64]

$$\lambda_{e-p} = \frac{1.04 + \mu^* \ln\left(\frac{\Theta_D}{1.45T_c}\right)}{(1 - 0.62\mu^*)\ln\left(\frac{\Theta_D}{1.45T_c}\right) - 1.04}$$

where μ^* is the screened Coulomb pseudopotential parameter, typically taken as $\mu^* = 0.13$[19] (in typical BCS superconductors, μ^* varies within a narrow range of 0.10–0.14, as evidenced both by theoretical estimations and experimental measurements).[65,66] Taking $T_c = 1.3$ K and $\Theta_D = 230$ K, we obtain $\lambda_{e\text{-}p} = 0.49$, which is slightly lower than $\lambda_{e\text{-}p}$ for an isoelectronic $LiPd_2Ge$ ($\lambda_{e\text{-}p} = 0.56$[39]). It is, however, worth noting that the estimation of $\lambda_{e\text{-}p}$ depends on the assumed value of μ^*. A relatively low value of the electron–phonon coupling constant as well as a small $\Delta C/\gamma T_c$ indicates that $LiPd_2Si$ is a weakly coupled BCS superconductor.

In addition, having the electron–phonon coupling constant and the Sommerfeld coefficient, the noninteracting density of states at the Fermi level DOS (E_F) can be estimated from

$$\text{DOS}\ (E_F) = \frac{3\gamma}{\pi^2 k_B^2 (1 + \lambda_{e-p})}$$

where k_B is the Boltzmann constant. The obtained DOS (E_F) = 1.5 states/eV/f.u. is in a reasonable agreement with the value of DOS (E_F) = 1.7 states/eV/f.u. from ab initio electronic structure calculations (see Figure 7).

Figure S3 in the Supporting Information shows the heat capacity measurements under applied magnetic fields. The magnitude of the discontinuity and the transition temperature decrease as the strength of the applied magnetic field is increased. The width of the transition also becomes broader in higher magnetic fields. The specific heat jumps ($\Delta C_p/T_c$) measured under zero-field and 50 Oe (the lowest applied field) are comparable, suggesting crossover from the first- to second-order phase transition, expected in type-I superconductors.[60,62,67,68]

https://doi.org/10.1021/acs.chemmater.3c02398
Chem. Mater. 2024, 36, 1870–1879

Figure 5b depicts the temperature dependence of critical field $H_c(T)$, with data points taken from the $C_p(T)$ measurements. The latest were used to the fit by a formula:

$$H_c(T) = H_c(0)\left[1 - \left(\frac{T}{T_c}\right)^2\right]$$

where T_c is the superconducting critical temperature, and $H_c(0)$ is the critical field at 0 K. The fit represented by a red solid line yields T_c = 1.30(2) K and a zero-temperature value of $H_c(0)$ = 326(8) Oe.

All of the extracted normal and superconducting state parameters are listed in Table 1.

Table 1. Comparison of the Physical Properties Reported for $LiPd_2Z$ (Z = Si, Ge, Sn)[a]

	$LiPd_2Si$	$LiPd_2Ge$[39]	$LiPd_2Sn$[39]
T_c (K) exp./predicted	1.3/0.76[39]	1.96/1.5	-[b]/0.25
$H_c(0)$ (Oe)	326(8)	342	-
γ	5.3(1)	5.8(1)	4.4(1)
$\lambda_{e\text{-}p}$[c]	0.49	0.56	-
Θ_D (K)	230(3)	194(3)	168(1)
DOS (E_F)[d]	1.52	1.60	-
$\Delta C/\gamma T_c$	1.1	1.38	-

[a]Data for $LiPd_2Ge$ are taken from ref 39. [b]"-" Superconductivity not observed down to T = 0.4 K. [c]Estimated, assuming μ^* = 0.13. [d]Estimated from the experimental values of T_c and $\lambda_{e\text{-}p}$.

The crystal orbital (CO) picture (Figure 6) of $LiPd_2Si$ can be described starting with a cubic Pd cage. The 4*d* and 5*s*

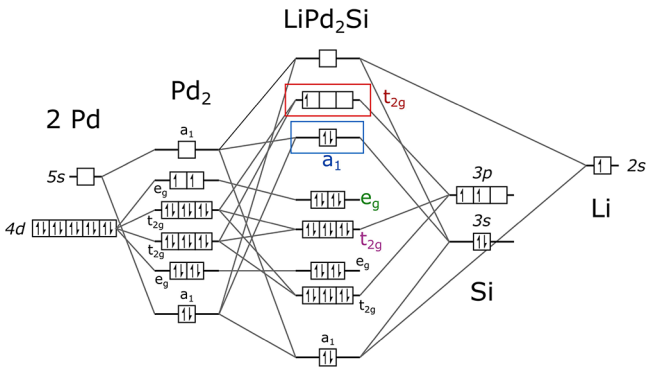

Figure 6. Crystal orbital scheme for $LiPd_2Si$, presenting the electronic structure of the Heusler phase as an effect of interaction between the cubic Pd cage (left) and the Si and Li atoms. A nondegenerate CO (blue), derived from antibonding Pd−Si *s* interaction, is highlighted in blue. These orbitals form the first branch of the Fermi surface (see Figure 7e). The triply degenerate antibonding Pd *d*−Si *p* orbital (red) contributes to the remaining two FS branches. Orbital labels are colored consistently with Figure 7. Note that in the extended solid, the two highlighted orbitals (a_1 and t_{2g}) are empty at the Γ point (Figure 7), but the bands formed by them remain partially filled in other parts of the Brillouin zone.

atomic orbitals (AOs) of Pd interact, forming an electronic "backbone" which is for the most part preserved in the complete Heusler phase. Cage orbitals of the e_g symmetry do not strongly interact with Si *s*/*p* and Li *s* AOs and form rather narrow bands below E_F. Si 3*p* interacts with Pd cage t_{2g} orbitals, changing the order of t_{2g} and e_g COs and forming a triply degenerate Pd *d*−Si *p* antibonding orbital (highlighted in red), which is populated by the single electron donated by Li.

This picture is consistent with the results of DFT calculations on $LiPd_2Si$ presented in Figure 7. The assumed

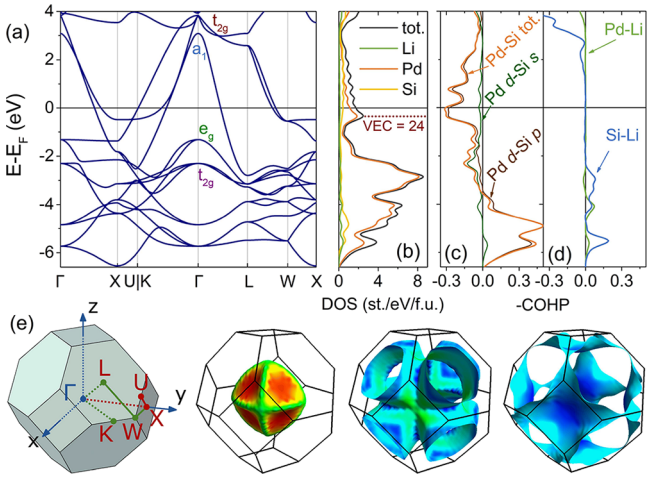

Figure 7. Results of DFT calculations of the electronic structure of $LiPd_2Si$. Panel (a) shows the band structure with three individual bands (their symmetry at the Γ point is labeled in red and blue) crossing the Fermi level, forming three hole-like Fermi surface branches. Two weakly dispersive sets of bands (labeled green and purple) can be derived from the crystal orbitals of the Pd cage (Figure 6). Labeling of high-symmetry points is shown in panel (e). Panel (b) shows the electronic DOS. The highest of the three broad peaks between E = −6 and −2 eV below E_F is contributed almost exclusively by Pd *d* states, while the lower two show a stronger Si contribution, in accordance with CO considerations (Figure 6). The DOS (E_F) = 1.7 states/eV/f.u. and is derived from the antibonding interaction of Pd and Si AOs, as shown in Panel (c). The negative value of −COHP for Pd *d* −Si *s*/*p* around E_F is consistent with the inferred antibonding character of the topmost occupied orbitals (Figure 6). Panel (d) shows the −COHP for Pd−Li and Si−Li pairs, suggesting that the antibonding Li-derived states lie well above E_F, consistent with the polar nature of Li-(Pd_2Si) bonding and highlighting the role of Li as an electron donor. Panel (e) shows the Brillouin zone (BZ) of a face-centered cubic lattice with high symmetry points shown in red (BZ center − Γ − in blue). Red and green lines are the paths through the BZ that were plotted in Panel (a). The three branches of FS are colored according to the increasing Fermi velocity from blue to red. The first branch derives from (Pd_2) a_1−Si *s*−Li s interaction, while the remaining two are from (Pd_2) t_2 -Si *p*.

order of COs agrees with the order of eigenvalues in the Brillouin zone (BZ) center Γ (Figure 7a). States ca. 2 eV below the Fermi level (E_F) are almost completely contributed by Pd, while the DOS (E_F) bears both strong Pd and Si contributions (Figure 7b). Li orbitals are mostly empty, with a peak of Li-derived DOS lying ca. 4 eV above E_F. The crystal orbital Hamilton population analysis (−COHP, Figure 7c,d) shows that the interactions of Pd and Si contributing to the DOS (E_F) are of an antibonding nature.

The topmost, partially filled t_{2g} CO forms the latter two of the three Fermi surface (FS) branches (see Figure 7a,e), while the first branch derives from a Pd−Si antibonding a_1 orbital (blue) resulting from the interaction of Pd cage a_1 orbital, Si 3*s* AO, and, to a lesser extent Li 2*s* AO. Li acts mostly as an electron donor to the CaF_2-type Pd_2Si sublattice, as evidenced by DOS and −COHP (Figure 7b,d). The calculated Bader charges are $Li^{+0.83}(Pd^{-0.61})_2Si^{+0.39}$, suggesting that in addition

https://doi.org/10.1021/acs.chemmater.3c02398
Chem. Mater. 2024, 36, 1870−1879

to a strong electron transfer from Li to Pd, the Si atom also donates electron density to the Pd cage.

$LiPd_2Si$ is one of the two Heusler superconductors (SCs) containing 25 valence electrons (1 + 2 × 10 + 4) per formula unit.[24] Most of the 34 Heusler SCs show valence electron count *VEC* = 26−29,[19,20,24,30,31] all of them featuring the same electronic "backbone" of Ni-, Pd-, Pt-, or Au-based cubic cage interacting with an electropositive early transition metal (TM) or lanthanide (only 3 *s*-block metal-bearing SC Heusler compounds are reported) and a *p*-block metal/metalloid. In the remaining two superconducting phases, $LiGa_2Rh$ and $LiGa_2Ir$[31,69] (both with VEC = 16), the cubic cage is built from *p*-block atoms resulting in a qualitatively distinct electronic structure.

Besides the lower electron count, the major difference between the $LiPd_2Si$ and the VEC = 27 superconducting compounds results from the difference of frontier orbitals of Li (*s*) and TM/lanthanide (*s* and *d*). This results in a singly degenerate orbital, which contributes to the Fermi surface. On the contrary, in the majority of Heusler superconductors where a transition metal or lanthanide atom occupies the 4*a* site, the a_1 orbital is much higher in energy, and its associated band does not cross the Fermi level (see Figure S4 of the Supporting Information for sample band structures of Heusler superconductors and Figure 8 for the band structure, DOS, COHP, and MO diagram of $HfPd_2Al$).

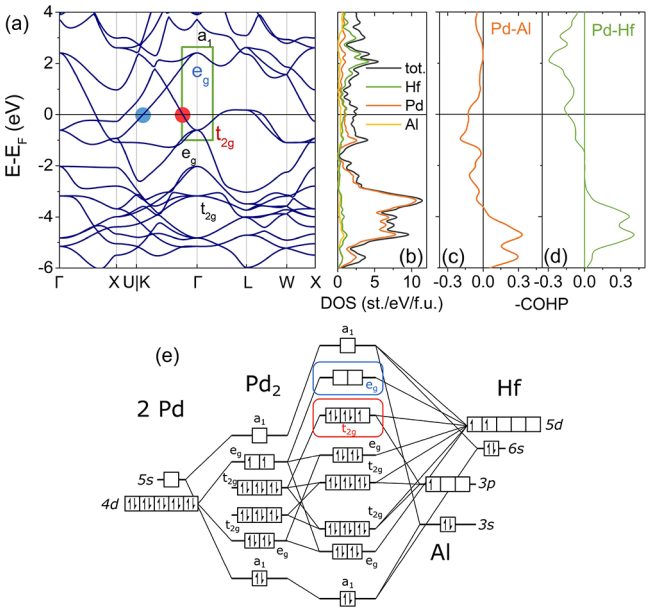

Figure 8. Panel (a) shows the calculated band structure of $HfPd_2Al$. There are three bands crossing the Fermi level (highlighted with a green rectangle): one derived from the e_g crystal orbital (blue; see also panel (e)), forming a set of hole pockets, and two electron-like derived from t_{2g} CO (red). Colored circles mark the points along the K-Γ line where the respective bands cross the Fermi level. As in $LiPd_2Si$ (Figure 7a), the two sets of weakly dispersive bands positioned below the Fermi level ($E - E_F$ from ca. −4 to −2 eV, labeled in black) can be derived from the Pd cage orbitals. The overall shape of the DOS (panel (b)) is similar to the $LiPd_2Si$ case; however, the DOS (E_F) has a significant Hf contribution (while the Li contribution to DOS (E_F) is negligible). COHP (c,d) shows that the bands crossing the Fermi level have Pd−Al and Pd−Hf antibonding characters. Panel (e) shows a crystal orbital scheme. Note that some of the high-energy (unoccupied) orbitals were omitted for clarity.

The difference between the electronic structures of $LiPd_2Si$ and $LiPd_2Ge$[39] (VEC = 25) and the remaining Heusler SCs is not merely due to electron count but rather stems from different bonding situations, making the two compounds a special subgroup of the Heusler SC family. Thus, considering just the frontier orbitals involved and the VEC, it may be interesting to investigate the $Mg(Ni,Pd,Pt)_2(Al,Ga,In)$ and $Li(Ni,Pt)_2(Si,Ge,Sn)$ phases as possible superconductors, especially since some of them were independently highlighted as possible superconductors in a recent machine learning study.[37] Moreover, there are several CaF_2-type compounds reported with VEC values close to 25. We believe that they might be driven to superconductivity by filling the voids with Li or Mg atoms (owing to their relatively small size). A good example is the Rh_2As phase[70] (VEC = 23), which is reported to superconduct below T_c = 1.1 K.[71] The OQMD database[72,73] predicts that its Li-bearing Heusler counterpart $LiRh_2As$ (id:450688; VEC = 24) is just slightly above the convex hull of Li−Rh−As (0.001 eV/atom). This suggests that the Heusler phase may be synthesizable. Tuning the VEC by adding Li would help to understand the details of the VEC-T_c behavior of Heusler compounds. $MgRh_2As$ (id:451326; VEC = 25) would likely be difficult to stabilize (convex hull distance: 0.127 eV/atom).

Keeping in mind the expected semiconducting behavior of VEC = 24 full Heusler compounds,[4] one may be tempted to see $LiPd_2Z$ (Z = Si, Ge, Sn) as a semiconductor/semimetal phase that is driven metallic and superconducting by increasing the electron count, a situation quite common among the known superconductor groups.[74,75] However, our electronic structure calculations contradict this simple yet admittedly elegant picture in two ways: (1) a rigid band calculation with an electron count decreased to 24 for $LiPd_2Si$ shows no band gap at or around the Fermi level (Figure 7b), and (2) the order of electronic states/crystal orbitals is different in $LiPd_2Si$ and VFe_2Al. As for (1), the calculated E_F for VEC = 24 would actually lie at a peak of DOS that results from a flat band along the U−X−W BZ path (Figure 7a,b), suggesting electronic instability. In the case of (2), the band gap appears in VFe_2Al between the fully occupied t_{2g} triplet and e_g doublet.[4] In $LiPd_2Si$, there are two frontier COs: a_1 and t_{2g}, derived from the Pd cage a_1 orbital interacting with Si *s* and Li *s* states, and two cage t_{2g} orbitals interacting with Si *p* states, respectively. Bands formed by both COs are partially filled, and a shift of the Fermi level that would result from a hypothetical removal of one electron per f.u. would only change the shape of the Fermi surface but not lead to a semiconducting behavior. The different order of COs derives from different frontier orbitals involved in the two compounds: V *d* states versus Li *s*. The importance of *d*−*d* interaction in the formation of band gap was extensively discussed in the literature for half Heusler phases.[76−78] We recently showed that due to the lack of *d*−*d* hybridization, *s*-metal bearing half Heusler phases including MgPdSb, MgAgAs (and others), are robustly metallic even at the "closed shell" electron count (VEC = 18).[79] Extension of the VEC−T_c relation to all known Heusler compounds is thus an oversimplification that neglects the differences in the bonding situation.

It is also worth noting that, while the "24-electron rule" helps to rationalize the semiconducting properties of VFe_2Al,[4] the number of reported *VEC* = 24 full Heusler compounds is limited to 5 (semiconducting VFe_2Al, VFe_2Ga[26,80,81] and

https://doi.org/10.1021/acs.chemmater.3c02398
Chem. Mater. 2024, 36, 1870−1879

$TiFe_2Sn$,[82] semimetallic $NbRu_2Al$,[83] and half-metallic ferromagnet WMn_2Sn[84,85]).

The Pd−Si states at the Fermi level are antibonding (Figure 7c). This supports the hypothesis that the occurrence of superconductivity is correlated with the occupation of antibonding electronic states,[74,86−93] leading to a kind of "electronic strain" that can also result in a structural distortion[94] or ferromagnetism.[95,96] This is consistent with the general observation that in many cases superconductivity arises when a crystal structure distortion (such as charge density wave order) or magnetic transition is suppressed by tuning a system using chemical doping or pressure.[75,97−99]

CONCLUSIONS

We have investigated the low-temperature physical properties of $LiPd_2Si$, which belongs to the Heusler family (space group $Fm\bar{3}m$, No. 225). According to ab initio calculations, $LiPd_2Si$ was expected to reveal superconducting behavior below T = 1 K.[39] Specific heat and magnetic measurements performed down to low temperatures prove bulk superconductivity below T_c = 1.3 K, which is higher than that predicted. $LiPd_2Si$ is, therefore, the second superconductor in the Heusler family containing 25 valence electrons.

Detailed studies of the superconducting properties show that $LiPd_2Si$ is a weakly coupled BCS superconductor with an electron−phonon coupling constant $\lambda_{e\text{-}p}$ = 0.49 and a heat capacity anomaly $\Delta C/\gamma T_c$ = 1.1. Moreover, as in the case of the isostructural $LiPd_2Ge$, our results of the field dependence of isothermal magnetizations suggest a type-I superconductivity in $LiPd_2Si$. We did not observe a superconducting transition in $LiPd_2Sn$ down to T = 0.4 K, in agreement with the earlier predictions.[39]

Almost all Heusler superconductors share the common structural motif of a Ni-, Pd-, Pt-, or Au-based cubic cage, with the overlapping *d* orbitals forming their electronic "backbone". However, the $LiPd_2Z$ (Z = Si, Ge)[39] and $MgPd_2Sb$[24] phases show distinctive features in the electronic structure when compared to the remaining Heusler superconductors. This is due to the fact that an *s*-block metal occupies the site that in other compounds is filled with an early transition metal or a rare-earth metal. While the rigid band approximation-based VEC−property relationship in Heusler compounds is a useful predictive tool,[4,19,24,100] one has to include another important factor which is the type of interacting frontier orbitals, as some of the Heusler system features depend strongly on the presence of *d*−*d* interaction within the CaF_2-type sublattice.

We postulate that VEC = 25 Heusler phases are interesting and largely unexplored candidates in the search for new superconducting intermetallic compounds.

ASSOCIATED CONTENT

Supporting Information

The Supporting Information is available free of charge at https://pubs.acs.org/doi/10.1021/acs.chemmater.3c02398.

XRD patterns of $LiPd_2Si$, unit cell, and crystal structure parameters for $LiPd_2Si$; low-temperature heat capacity under applied magnetic fields; and band structures of YPd_2In, $LuPt_2In$, $ZrNi_2Ga$, and $HfPd_2Al$ Heusler compounds (PDF)

AUTHOR INFORMATION

Corresponding Authors

Tomasz Klimczuk − *Faculty of Applied Physics and Mathematics and Advanced Materials Centre, Gdansk University of Technology, 80-233 Gdańsk, Poland;* orcid.org/0000-0002-7089-4631; Email: tomasz.klimczuk@pg.edu.pl

Michał J. Winiarski − *Faculty of Applied Physics and Mathematics and Advanced Materials Centre, Gdansk University of Technology, 80-233 Gdańsk, Poland;* orcid.org/0000-0001-9083-8066; Email: michal.winiarski@pg.edu.pl

Authors

Karolina Górnicka − *Faculty of Applied Physics and Mathematics and Advanced Materials Centre, Gdansk University of Technology, 80-233 Gdańsk, Poland*

Xin Gui − *Department of Chemistry, Princeton University, Princeton, New Jersey 08540, United States;* Present Address: Department of Chemistry, University of Pittsburgh, Pittsburgh, Pennsylvania 15260, United States; orcid.org/0000-0003-0616-2150

Juan R. Chamorro − *Materials Department and Materials Research Laboratory, University of California, Santa Barbara, Santa Barbara, California 93106, United States*

Tyrel M. McQueen − *Department of Chemistry, William H. Miller III Department of Physics and Astronomy, Department of Materials Science and Engineering, and Institute for Quantum Matter, Johns Hopkins University, Baltimore, Maryland 21218, United States;* orcid.org/0000-0002-8493-4630

Robert J. Cava − *Department of Chemistry, Princeton University, Princeton, New Jersey 08540, United States*

Complete contact information is available at: https://pubs.acs.org/10.1021/acs.chemmater.3c02398

Author Contributions

The manuscript was written through contributions of all authors.

Notes

The authors declare no competing financial interest.

ACKNOWLEDGMENTS

Work at Gdańsk University of Technology was supported by the National Science Centre (Poland), grant no. UMO-2018/30/M/ST5/000773. The work at Princeton was supported by the US Department of Energy, Basic Energy Sciences, grant DE-FG02-98ER45706.The MPMS 3 system used for magnetic characterization was funded by the National Science Foundation, Division of Materials Research, Major Research Instrumentation Program, under grant no. 1828490.

ABBREVIATIONS

AO, atomic orbital; BCC, body-centered cubic structure; BCS, Bardeen−Cooper−Schriefer theory; BFGS, Broyden−Fletcher−Goldfarb−Shanno algorithm; CO, crystal orbital; DFT, density functional theory; DOS, density of (electronic) states; FC, field cooled; FCC, face-centered cubic structure; FS, Fermi surface; MO, molecular orbital; PBE GGA, Perdew−Burke−Ernzerhof generalized gradient approximation; SC, superconductor; VEC, valence electron count; XRD, X-ray diffraction; ZFC, zero-field cooled

REFERENCES

(1) Heusler, F. *Verh. Deutsch. Phys. Ges.* **1903**, *5*, 219.
(2) Dshemuchadse, J.; Steurer, W. More Statistics on Intermetallic Compounds − Ternary Phases. *Acta Cryst. A* **2015**, *71* (3), 335−345.
(3) Graf, T.; Parkin, S. S. P.; Felser, C. Heusler Compounds—A Material Class With Exceptional Properties. *IEEE Trans. Magn.* **2011**, *47* (2), 367−373.
(4) Graf, T.; Felser, C.; Parkin, S. S. P. Simple Rules for the Understanding of Heusler Compounds. *Prog. Solid State Chem.* **2011**, *39* (1), 1−50.
(5) Palmstrøm, C. J. Heusler Compounds and Spintronics. *Prog. Cryst. Growth Charact. Mater.* **2016**, *62* (2), 371−397.
(6) Anand, S.; Wood, M.; Xia, Y.; Wolverton, C.; Snyder, G. J. Double Half-Heuslers. *Joule* **2019**, *3* (5), 1226−1238.
(7) Drews, J.; Eberz, U.; Schuster, H.-U. Optische Untersuchungen an farbigen Intermetallischen phasen. *J. Less Common Met.* **1986**, *116* (1), 271−278.
(8) Dai, X.; Liu, G.; Fecher, G. H.; Felser, C.; Li, Y.; Liu, H. New Quarternary Half Metallic Material CoFeMnSi. *J. Appl. Phys.* **2009**, *105* (7), No. 07E901.
(9) Dshemuchadse, J.; Steurer, W. Some Statistics on Intermetallic Compounds. *Inorg. Chem.* **2015**, *54* (3), 1120−1128.
(10) Shan, R.; Sukegawa, H.; Wang, W. H.; Kodzuka, M.; Furubayashi, T.; Ohkubo, T.; Mitani, S.; Inomata, K.; Hono, K. Demonstration of Half-Metallicity in Fermi-Level-Tuned Heusler Alloy $Co_2FeAl_{0.5}Si_{0.5}$ at Room Temperature. *Phys. Rev. Lett.* **2009**, *102* (24), No. 246601.
(11) Felser, C.; Wollmann, L.; Chadov, S.; Fecher, G. H.; Parkin, S. S. P. Basics and Prospective of Magnetic Heusler Compounds. *APL Mater.* **2015**, *3* (4), No. 041518.
(12) Takayanagi, S.; Woods, S. B.; Wada, N.; Watanabe, T.; Ōnuki, Y.; Kobori, A.; Komatsubara, T.; Imai, M.; Asano, H. Magnetic and Transport Properties in the Cubic Heavy Fermion System $CeInCu_2$. *J. Magn. Magn. Mater.* **1988**, *76−77*, 281−282.
(13) Nakamura, H.; Kitaoka, Y.; Asayama, K.; Ōnuki, Y.; Komatsubara, T. Observation of Two Phase Transitions in the Heusler Heavy Fermion System $CeInCu_2$. *J. Magn. Magn. Mater.* **1988**, *76−77*, 467−468.
(14) Lahiouel, R.; Pierre, J.; Siaud, E.; Galera, R. M.; Besnus, M. J.; Kappler, J. P.; Murani, A. P. Kondo Lattice and Heavy Fermions in Heusler Phases: $CeInAg_{2-x}Cu_x$. *Z. Phys. B* **1987**, *67* (2), 185−191.
(15) Gofryk, K.; Kaczorowski, D.; Czopnik, A. Magnetic and Transport Properties of UPd_2Sb. *Solid State Commun.* **2005**, *133* (10), 625−628.
(16) Kaczorowski, D.; Leithe-Jasper, A.; Cichorek, T.; Tenya, K.; Custers, J.; Gegenwart, P.; Grin, Y. Possible Heavy-Fermion Behavior in a Heusler-Type Compound $YbPd_2Sb$. *Acta Phys. Pol. B.* **2003**, *34*, 1253.
(17) Liu, Z. H.; Zhang, M.; Cui, Y. T.; Zhou, Y. Q.; Wang, W. H.; Wu, G. H.; Zhang, X. X.; Xiao, G. Martensitic Transformation and Shape Memory Effect in Ferromagnetic Heusler Alloy Ni_2FeGa. *Appl. Phys. Lett.* **2003**, *82* (3), 424−426.
(18) de Paula, V. G.; Reis, M. S. All-d-Metal Full Heusler Alloys: A Novel Class of Functional Materials. *Chem. Mater.* **2021**, *33* (14), 5483−5495.
(19) Klimczuk, T.; Wang, C. H.; Gofryk, K.; Ronning, F.; Winterlik, J.; Fecher, G. H.; Griveau, J.-C.; Colineau, E.; Felser, C.; Thompson, J. D.; et al. Superconductivity in the Heusler Family of Intermetallics. *Phys. Rev. B* **2012**, *85* (17), No. 174505.
(20) Winterlik, J.; Fecher, G. H.; Thomas, A.; Felser, C. Superconductivity in Palladium-Based Heusler Compounds. *Phys. Rev. B* **2009**, *79* (6), No. 064508.
(21) Wernick, J. H.; Hull, G. W.; Geballe, T. H.; Bernardini, J. E.; Waszczak, J. V. Superconductivity in Ternary Heusler Intermetallic Compounds. *Mater. Lett.* **1983**, *2* (2), 90−92.
(22) Pavlosiuk, O.; Kaczorowski, D.; Wiśniewski, P. Shubnikov - de Haas Oscillations, Weak Antilocalization Effect and Large Linear Magnetoresistance in the Putative Topological Superconductor LuPdBi. *Sci. Rep.* **2015**, *5*, 9158.
(23) Pavlosiuk, O.; Kaczorowski, D.; Wiśniewski, P. Superconductivity and Shubnikov–de Haas Oscillations in the Noncentrosymmetric Half-Heusler Compound YPtBi. *Phys. Rev. B* **2016**, *94* (3), No. 035130.
(24) Winiarski, M. J.; Kuderowicz, G.; Górnicka, K.; Litzbarski, L. S.; Stolecka, K.; Wiendlocha, B.; Cava, R. J.; Klimczuk, T. $MgPd_2Sb$: A Mg-Based Heusler-Type Superconductor. *Phys. Rev. B* **2021**, *103* (21), No. 214501.
(25) Mayer, J. A.; Seshadri, R. Electron Count Dictates Phase Separation in Heusler Alloys. *Phys. Rev. Mater.* **2022**, *6* (5), No. 054406.
(26) Nishino, Y.; Kato, M.; Asano, S.; Soda, K.; Hayasaki, M.; Mizutani, U. Semiconductorlike Behavior of Electrical Resistivity in Heusler-Type Fe_2VAl Compound. *Phys. Rev. Lett.* **1997**, *79* (10), 1909−1912.
(27) Singh, D. J.; Mazin, I. I. Electronic Structure, Local Moments, and Transport in Fe2VAl. *Phys. Rev. B* **1998**, *57* (22), 14352−14356.
(28) Feng, Y.; Rhee, J. Y.; Wiener, T. A.; Lynch, D. W.; Hubbard, B. E.; Sievers, A. J.; Schlagel, D. L.; Lograsso, T. A.; Miller, L. L. Physical Properties of Heusler-like Fe_2VAl. *Phys. Rev. B* **2001**, *63* (16), No. 165109.
(29) Garmroudi, F.; Parzer, M.; Riss, A.; Ruban, A. V.; Khmelevskyi, S.; Reticcioli, M.; Knopf, M.; Michor, H.; Pustogow, A.; Mori, T.; et al. Anderson Transition in Stoichiometric Fe_2VAl: High Thermoelectric Performance from Impurity Bands. *Nat. Commun.* **2022**, *13* (1), 3599.
(30) DeStefano, J. M.; Marciaga, G. P.; Flahavan, J. B.; Shah, U. S.; Elmslie, T. A.; Meisel, M. W.; Hamlin, J. J. Absence of Superconductivity in Topological Metal $ScInAu_2$. *Physica C* **2021**, *589*, 1353928.
(31) Górnicka, K.; Kuderowicz, G.; Winiarski, M. J.; Wiendlocha, B.; Klimczuk, T. Superconductivity in $LiGa_2Ir$ Heusler Type Compound with VEC = 16. *Sci. Rep.* **2021**, *11* (1), 16517.
(32) Matthias, B. T. Transition Temperatures of Superconductors. *Phys. Rev.* **1953**, *92* (4), 874−876.
(33) Matthias, B. T. Empirical Relation between Superconductivity and the Number of Valence Electrons per Atom. *Phys. Rev.* **1955**, *97* (1), 74−76.
(34) Conder, K. A Second Life of the Matthias's Rules. *Supercond. Sci. Technol.* **2016**, *29* (8), No. 080502.
(35) Stolze, K.; Cevallos, F. A.; Kong, T.; Cava, R. J. High-Entropy Alloy Superconductors on an α-Mn Lattice. *J. Mater. Chem. C* **2018**, *6* (39), 10441−10449.
(36) h Sun, L.; Cava, R. J. High-Entropy Alloy Superconductors: Status, Opportunities, and Challenges. *Phys. Rev. Mater.* **2019**, *3* (9), No. 090301.
(37) Pogue, E. A.; New, A.; McElroy, K.; Le, N. Q.; Pekala, M. J.; McCue, I.; Gienger, E.; Domenico, J.; Hedrick, E.; McQueen, T. M.; et al. Closed-Loop Superconducting Materials Discovery. *npj Comput. Mater.* **2023**, *9* (1), 181.
(38) Poole, C. P.; Farach, H. A. Tabulations and Correlations of Transition Temperatures of Classical Superconductors. *J. Supercond.* **2000**, *13* (1), 47−60.
(39) Górnicka, K.; Kuderowicz, G.; Carnicom, E. M.; Kutorasiński, K.; Wiendlocha, B.; Cava, R. J.; Klimczuk, T. Soft-Mode Enhanced Type-I Superconductivity in $LiPd_2Ge$. *Phys. Rev. B* **2020**, *102* (2), No. 024507.
(40) Kistrup, C.-J.; Schuster, H.-U. Neue Ternäre Phasen von Platinmetallen Mit Lithium Und Elementen Der 4. Hauptgruppe/ New Ternary Phases of the Platingroup-Metals with Lithium and Elements of the 4 b-Group. *Z. Naturforsch. B* **1972**, *27* (3), 324−325.
(41) Corti, C. W.; van der Lingen, E. Special Colors of Precious-Metal Jewelry: Present and Future. In *Proceedings of the Thirtieth Santa Fe Symposium on Jewelry Manufacturing Technology*; Met-Chem Research: Albuquerque, NM, 2016; pp 165−197.
(42) Giannozzi, P.; Baroni, S.; Bonini, N.; Calandra, M.; Car, R.; Cavazzoni, C.; Ceresoli, D.; Chiarotti, G. L.; Cococcioni, M.; Dabo, I.; Corso, A. D.; et al. QUANTUM ESPRESSO: A Modular and

https://doi.org/10.1021/acs.chemmater.3c02398
Chem. Mater. 2024, 36, 1870−1879

Open-Source Software Project for Quantum Simulations of Materials. *J. Phys.: Condens. Matter* **2009**, *21* (39), No. 395502.
(43) Giannozzi, P.; Andreussi, O.; Brumme, T.; Bunau, O.; Nardelli, M. B.; Calandra, M.; Car, R.; Cavazzoni, C.; Ceresoli, D.; Cococcioni, M.; et al. Advanced Capabilities for Materials Modelling with Quantum ESPRESSO. *J. Phys.: Condens. Matter* **2017**, *29* (46), 465901.
(44) Giannozzi, P.; Baseggio, O.; Bonfà, P.; Brunato, D.; Car, R.; Carnimeo, I.; Cavazzoni, C.; de Gironcoli, S.; Delugas, P.; Ferrari Ruffino, F.; et al. Quantum ESPRESSO toward the Exascale. *J. Chem. Phys.* **2020**, *152* (15), 154105.
(45) Perdew, J. P.; Burke, K.; Ernzerhof, M. Generalized Gradient Approximation Made Simple. *Phys. Rev. Lett.* **1996**, *77* (18), 3865−3868.
(46) Blöchl, P. E. Projector Augmented-Wave Method. *Phys. Rev. B* **1994**, *50* (24), 17953−17979.
(47) Kresse, G.; Joubert, D. From Ultrasoft Pseudopotentials to the Projector Augmented-Wave Method. *Phys. Rev. B* **1999**, *59* (3), 1758−1775.
(48) Dal Corso, A. Pseudopotentials Periodic Table: From H to Pu. *Comput. Mater. Sci.* **2014**, *95*, 337−350.
(49) Dronskowski, R.; Bloechl, P. E. Crystal Orbital Hamilton Populations (COHP): Energy-Resolved Visualization of Chemical Bonding in Solids Based on Density-Functional Calculations. *J. Phys. Chem.* **1993**, *97* (33), 8617−8624.
(50) Steinberg, S.; Dronskowski, R. The Crystal Orbital Hamilton Population (COHP) Method as a Tool to Visualize and Analyze Chemical Bonding in Intermetallic Compounds. *Crystals* **2018**, *8* (5), 225.
(51) Maintz, S.; Deringer, V. L.; Tchougréeff, A. L.; Dronskowski, R. Analytic Projection from Plane-Wave and PAW Wavefunctions and Application to Chemical-Bonding Analysis in Solids. *J. Comput. Chem.* **2013**, *34* (29), 2557−2567.
(52) Maintz, S.; Deringer, V. L.; Tchougréeff, A. L.; Dronskowski, R. LOBSTER: A Tool to Extract Chemical Bonding from Plane-Wave Based DFT. *J. Comput. Chem.* **2016**, *37* (11), 1030−1035.
(53) Koga, T.; Kanayama, K.; Watanabe, S.; Thakkar, A. J. Analytical Hartree−Fock Wave Functions Subject to Cusp and Asymptotic Constraints: He to Xe, Li^+ to Cs^+, H^- to I^-. *Int. J. Quantum Chem.* **1999**, *71* (6), 491−497.
(54) Henkelman, G.; Arnaldsson, A.; Jónsson, H. A Fast and Robust Algorithm for Bader Decomposition of Charge Density. *Comput. Mater. Sci.* **2006**, *36* (3), 354−360.
(55) Sanville, E.; Kenny, S. D.; Smith, R.; Henkelman, G. Improved grid-based algorithm for Bader charge allocation. *J. Comput. Chem.* **2007**, *28* (5), 899−908.
(56) Tang, W.; Sanville, E.; Henkelman, G. A Grid-Based Bader Analysis Algorithm without Lattice Bias. *J. Phys.: Condens. Matter* **2009**, *21* (8), No. 084204.
(57) Jain, A.; Ong, S. P.; Hautier, G.; Chen, W.; Richards, W. D.; Dacek, S.; Cholia, S.; Gunter, D.; Skinner, D.; Ceder, G.; et al. Commentary: The Materials Project: A Materials Genome Approach to Accelerating Materials Innovation. *APL Mater.* **2013**, *1* (1), No. 011002.
(58) Ong, S. P.; Richards, W. D.; Jain, A.; Hautier, G.; Kocher, M.; Cholia, S.; Gunter, D.; Chevrier, V. L.; Persson, K. A.; Ceder, G. Python Materials Genomics (Pymatgen): A Robust, Open-Source Python Library for Materials Analysis. *Comput. Mater. Sci.* **2013**, *68*, 314−319.
(59) Klimczuk, T.; Cava, R. J. The Effect of Fe and Ru Substitution on the Superconductivity in $MgCNi_3$. *Solid State Commun.* **2004**, *132* (6), 379−382.
(60) Sun, S.; Liu, K.; Lei, H. Type-I Superconductivity in KBi_2 Single Crystals. *J. Phys.: Condens. Matter* **2016**, *28* (8), No. 085701.
(61) Svanidze, E.; Morosan, E. Type-I Superconductivity in $ScGa_3$ and $LuGa_3$ Single Crystals. *Phys. Rev. B* **2012**, *85* (17), No. 174514.
(62) Górnicka, K.; Gutowska, S.; Winiarski, M. J.; Wiendlocha, B.; Xie, W.; Cava, R. J.; Klimczuk, T. Superconductivity on a Bi Square Net in LiBi. *Chem. Mater.* **2020**, *32* (7), 3150−3159.
(63) Peets, D. C.; Cheng, E.; Ying, T.; Kriener, M.; Shen, X.; Li, S.; Feng, D. Type-I Superconductivity in Al6Re. *Phys. Rev. B* **2019**, *99* (14), No. 144519.
(64) McMillan, W. L. Transition Temperature of Strong-Coupled Superconductors. *Phys. Rev.* **1968**, *167* (2), 331−344.
(65) Szczęśniak, R. On the Coulomb Pseudopotential for Al and Pb Superconductors. *Phys. Status Solidi B* **2007**, *244* (7), 2538−2542.
(66) Bauer, J.; Han, J. E.; Gunnarsson, O. Retardation Effects and the Coulomb Pseudopotential in the Theory of Superconductivity. *Phys. Rev. B* **2013**, *87* (5), No. 054507.
(67) Singh, Y.; Niazi, A.; Vannette, M. D.; Prozorov, R.; Johnston, D. C. Superconducting and Normal-State Properties of the Layered Boride OsB_2. *Phys. Rev. B* **2007**, *76* (21), No. 214510.
(68) Singh, J.; Jayaraj, A.; Srivastava, D.; Gayen, S.; Thamizhavel, A.; Singh, Y. Possible Multigap Type-I Superconductivity in the Layered Boride RuB_2. *Phys. Rev. B* **2018**, *97* (5), No. 054506.
(69) Carnicom, E. M.; Xie, W.; Yang, Z.; Górnicka, K.; Kong, T.; Klimczuk, T.; Cava, R. J. Importance of Specific Heat Characterization When Reporting New Superconductors: An Example of Superconductivity in $LiGa_2Rh$. *Chem. Mater.* **2019**, *31* (6), 2164−2173.
(70) Kjekshus, A.; Skaug, K. E.; Sæthre, L. J.; Sjöstrand, E.; Svensson, S. On the Phases Cr_2As, Fe_2As, Co_2As, and Rh_2As. *Acta Chem. Scand.* **1972**, *26*, 2554−2556.
(71) Roberts, B. W. Survey of Superconductive Materials and Critical Evaluation of Selected Properties. *J. Phys. Chem. Ref. Data* **1976**, *5* (3), 581−822.
(72) Saal, J. E.; Kirklin, S.; Aykol, M.; Meredig, B.; Wolverton, C. Materials Design and Discovery with High-Throughput Density Functional Theory: The Open Quantum Materials Database (OQMD). *JOM* **2013**, *65* (11), 1501−1509.
(73) Kirklin, S.; Saal, J. E.; Meredig, B.; Thompson, A.; Doak, J. W.; Aykol, M.; Rühl, S.; Wolverton, C. The Open Quantum Materials Database (OQMD): Assessing the Accuracy of DFT Formation Energies. *npj Comput. Mater.* **2015**, *1*, 15010.
(74) Ryżyńska, Z.; Chamorro, J. R.; McQueen, T. M.; Wiśniewski, P.; Kaczorowski, D.; Xie, W.; Cava, R. J.; Klimczuk, T.; Winiarski, M. J. $RuAl_6$—An Endohedral Aluminide Superconductor. *Chem. Mater.* **2020**, *32* (9), 3805−3812.
(75) Gui, X.; Lv, B.; Xie, W. Chemistry in Superconductors. *Chem. Rev.* **2021**, *121* (5), 2966−2991.
(76) Galanakis, I.; Dederichs, P. H.; Papanikolaou, N. Origin and Properties of the Gap in the Half-Ferromagnetic Heusler Alloys. *Phys. Rev. B* **2002**, *66* (13), No. 134428.
(77) Galanakis, I.; Mavropoulos, P.; Dederichs, P. H. Electronic Structure and Slater−Pauling Behaviour in Half-Metallic Heusler Alloys Calculated from First Principles. *J. Phys. D: Appl. Phys.* **2006**, *39* (5), 765.
(78) Yan, F.; Zhang, X.; Yu, Y. G.; Yu, L.; Nagaraja, A.; Mason, T. O.; Zunger, A. Design and Discovery of a Novel Half-Heusler Transparent Hole Conductor Made of All-Metallic Heavy Elements. *Nat. Commun.* **2015**, *6* (1), 7308.
(79) Winiarski, M. J.; Stolecka, K.; Litzbarski, L.; Tran, T. T.; Górnicka, K.; Klimczuk, T. MgPdSb—An Electron-Deficient Half-Heusler Phase. *J. Phys. Chem. C* **2022**, *126* (33), 14229−14235.
(80) Kawamiya, N.; Nishino, Y.; Matsuo, M.; Asano, S. Electrical-Resistance Maximum near the Curie Point in $(Fe_{1-x}V_x)_3Ga$ and $(Fe_{1-x}Ti_x)_3Ga$. *Phys. Rev. B* **1991**, *44* (22), 12406−12412.
(81) Ooiwa, K.; Endo, K. Nuclear Magnetic Relaxation in Heusler Alloys Fe_2VGa and Fe_2VAl. *J. Magn. Magn. Mater.* **1998**, *177*−*181*, 1443−1444.
(82) Buffon, M. L. C.; Laurita, G.; Lamontagne, L.; Levin, E. E.; Mooraj, S.; Lloyd, D. L.; White, N.; Pollock, T. M.; Seshadri, R. Thermoelectric Performance and the Role of Anti-Site Disorder in the 24-Electron Heusler $TiFe_2Sn$. *J. Phys.: Condens. Matter* **2017**, *29* (40), 405702.
(83) Mondal, S.; Mazumdar, C.; Ranganathan, R.; Alleno, E.; Sreeparvathy, P. C.; Kanchana, V.; Vaitheeswaran, G. Ferromagnetically Correlated Clusters in Semimetallic Ru_2NbAl Heusler Alloy and

https://doi.org/10.1021/acs.chemmater.3c02398
Chem. Mater. 2024, 36, 1870−1879

Its Thermoelectric Properties. *Phys. Rev. B* **2018**, *98* (20), No. 205130.
(84) van Engen, P. G.; Buschow, K. H. J.; Erman, M. Magnetic Properties and Magneto-Optical Spectroscopy of Heusler Alloys Based on Transition Metals and Sn. *J. Magn. Magn. Mater.* **1983**, *30* (3), 374−382.
(85) Rauf, S.; Arif, S.; Haneef, M.; Amin, B. The First Principle Study of Magnetic Properties of Mn_2WSn, Fe_2YSn (Y = Ti, V), Co_2YSn (Y = Ti, Zr, Hf, V, Mn) and Ni_2YSn (Y = Ti, Zr, Hf, V, Mn) Heusler Alloys. *J. Phys. Chem. Sol.* **2015**, *76*, 153−169.
(86) Neilson, J. R.; McQueen, T. M. Bonding, Ion Mobility, and Rate-Limiting Steps in Deintercalation Reactions with $ThCr_2Si_2$-Type KNi_2Se_2. *J. Am. Chem. Soc.* **2012**, *134* (18), 7750−7757.
(87) Neilson, J. R.; Llobet, A.; Stier, A. V.; Wu, L.; Wen, J.; Tao, J.; Zhu, Y.; Tesanovic, Z. B.; Armitage, N. P.; McQueen, T. M. Mixed-Valence-Driven Heavy-Fermion Behavior and Superconductivity in KNi_2Se_2. *Phys. Rev. B* **2012**, *86* (5), No. 054512.
(88) Neilson, J. R.; McQueen, T. M.; Llobet, A.; Wen, J.; Suchomel, M. R. Charge Density Wave Fluctuations, Heavy Electrons, and Superconductivity in KNi_2S_2. *Phys. Rev. B* **2013**, *87* (4), No. 045124.
(89) Xie, W.; Luo, H.; Baroudi, K.; Krizan, J. W.; Phelan, B. F.; Cava, R. J. Fragment-Based Design of NbRuB as a New Metal-Rich Boride Superconductor. *Chem. Mater.* **2015**, *27* (4), 1149−1152.
(90) Gui, X.; Sobczak, Z.; Chang, T.-R.; Xu, X.; Huang, A.; Jia, S.; Jeng, H.-T.; Klimczuk, T.; Xie, W. Superconducting SrSnP with Strong Sn−P Antibonding Interaction: Is the Sn Atom Single or Mixed Valent? *Chem. Mater.* **2018**, *30* (17), 6005−6013.
(91) Blawat, J.; Swatek, P. W.; Das, D.; Kaczorowski, D.; Jin, R.; Xie, W. Pd-P Antibonding Interactions in APd_2P_2 (A = Ca and Sr) Superconductors. *Phys. Rev. Mater.* **2020**, *4* (1), No. 014801.
(92) Verchenko, V. Y.; Tsirlin, A. A.; Shevelkov, A. V. Semiconducting and Superconducting Mo−Ga Frameworks: Total Energy and Chemical Bonding. *Inorg. Chem. Front.* **2021**, *8*, 1702−1709.
(93) Ryżyńska, Z.; Wiśniewski, P.; Kaczorowski, D.; Xie, W.; Cava, R. J.; Klimczuk, T.; Winiarski, M. J. Superconductivity in the Endohedral Ga Cluster Compound $PdGa_5$. *J. Phys. Chem. C* **2021**, *125* (20), 11294−11299.
(94) Decker, A.; Landrum, G. A.; Dronskowski, R. Structural and Electronic Peierls Distortions in the Elements (A): The Crystal Structure of Tellurium. *Z. Anorg. Allgem. Chem.* **2002**, *628* (1), 295−302.
(95) Dronskowski, R.; Korczak, K.; Lueken, H.; Jung, W. Chemically Tuning between Ferromagnetism and Antiferromagnetism by Combining Theory and Synthesis in Iron/Manganese Rhodium Borides. *Angew. Chem., Int. Ed.* **2002**, *41* (14), 2528−2532.
(96) Fokwa, B. P. T.; Lueken, H.; Dronskowski, R. Rational Synthetic Tuning between Itinerant Antiferromagnetism and Ferromagnetism in the Complex Boride Series $Sc_2FeRu_{5-n}Rh_nB_2$ ($0 \leq n \leq 5$). *Chem. − Eur. J.* **2007**, *13* (21), 6040−6046.
(97) Wagner, K. E.; Morosan, E.; Hor, Y. S.; Tao, J.; Zhu, Y.; Sanders, T.; McQueen, T. M.; Zandbergen, H. W.; Williams, A. J.; West, D. V.; et al. Tuning the Charge Density Wave and Superconductivity in Cu_xTaS_2. *Phys. Rev. B* **2008**, *78* (10), No. 104520.
(98) Das, T.; Panagopoulos, C. Two Types of Superconducting Domes in Unconventional Superconductors. *New J. Phys.* **2016**, *18* (10), No. 103033.
(99) Zhang, Z.; Chen, Z.; Zhou, Y.; Yuan, Y.; Wang, S.; Wang, J.; Yang, H.; An, C.; Zhang, L.; Zhu, X.; Zhou, Y.; Chen, X.; Zhou, J.; Yang, Z. Pressure-Induced Reemergence of Superconductivity in the Topological Kagome Metal CsV_3Sb_5. *Phys. Rev. B* **2021**, *103* (22), No. 224513.
(100) Kautzsch, L.; Mende, F.; Fecher, G. H.; Winterlik, J.; Felser, C. Are AuPdTM (T = Sc, Y and M = Al, Ga, In), Heusler Compounds Superconductors without Inversion Symmetry? *Materials* **2019**, *12* (16), 2580.

https://doi.org/10.1021/acs.chemmater.3c02398
Chem. Mater. 2024, 36, 1870−1879